2010

THE RADIO PROPERTIES AND MAGNETIC FIELD CONFIGURATION IN THE CRAB-LIKE PULSAR WIND NEBULA G54.1+0.3

CC Lang

QD Wang
University of Massachusetts - Amherst

F Lu

KI Clubb

Recommended Citation

The Radio Properties and Magnetic Field Configuration in the Crab-like Pulsar Wind Nebula G54.1+0.3

Cornelia C. Lang

Department of Physics & Astronomy, 703 Van Allen Hall, University of Iowa, Iowa City, IA 52242

cornelia-lang@uiowa.edu

Q. Daniel Wang

Department of Astronomy, University of Massachusetts, Amherst, MA 01002

Fangjun Lu[1]

Key Laboratory for Particle Astrophysics, Institute of High Energy Physics, Chinese Academy of Sciences, Beijing 100049, China

and

Kelsey I. Clubb[2]

Department of Physics & Astronomy, Van Allen Hall, University of Iowa, Iowa City, IA 52242

ABSTRACT

We present a multifrequency radio investigation of the Crab-like pulsar wind nebula (PWN) G54.1+0.3 using the Very Large Array. The high resolution of the observations reveals that G54.1+0.3 has a complex radio structure which includes filamentary and loop-like structures that are magnetized, a diffuse extent similar to the associated diffuse X-ray emission. But the radio and X-ray structures in the central region differ strikingly, indicating that they trace very different forms of particle injection from the pulsar and/or particle acceleration in the nebula. No spectral index gradient is detected in the radio emission across the PWN, whereas the X-ray emission softens outward in the nebula. The extensive radio polarization allows us to image in detail the intrinsic magnetic field, which is well-ordered and reveals that a number of loop-like filaments are

---

[1]Department of Astronomy, University of Massachusetts, Amherst, MA 01002

[2]Now at: Department of Physics and Astronomy, San Francisco State University 1600 Holloway Avenue, San Francisco, CA 94132

strongly magnetized. In addition, we determine that there are both radial and toroidal components to the magnetic field structure of the pulsar wind nebula. Strong mid-IR emission detected in *Spitzer* Space Telescope data is closely correlated with the radio emission arising from the southern edge of G54.1+0.3. In particular, the distributions of radio and X-ray emission compared with the mid-IR emission suggest that the PWN may be interacting with this interstellar cloud. This may be the first PWN where we are directly detecting its interplay with an interstellar cloud that has survived the impact of the supernova explosion associated with the pulsar's progenitor.

Subject headings: ISM: Individual: Alphanumeric: G54.1+0.3, ISM: Supernova Remnants

1.   Introduction

Crab-like supernova remnants, also known as pulsar wind nebulae (PWNe), provide unique laboratories for studying the interaction between high-energy pulsar wind materials and supernova ejecta. The synchrotron emission (normally observed at radio and X-ray wavelengths) arises from ultra-relativistic particles in reverse-shocked pulsar wind materials (Rees & Gunn 1974; Reynolds & Chevalier 1984). SNR G54.1+0.3 (or hereafter, G54.1+0.3) is considered to be a Crab-like source and we will refer to it and other similar objects as PWNe. Recent high-resolution *Chandra* observations ($1''$ or better) have revealed physical features similar to the Crab: a bright X-ray ring surrounding a central point source (corresponding to a 136 ms pulsar; Camilo et al. 2002), a western jet perpendicular to the ring, and an eastern protrusion, all in addition to the known low-brightness, diffuse component (Lu et al. 2002). The X-ray spectra of the above features are all nonthermal and steepen with increasing distance from the central pulsar, indicating significant particle energy evolution. The distance to G54.1+0.3 has been recently revisited by an HI absorption and ^{13}CO emission study (Leahy et al. 2008), which suggests that the distance to the PWN is approximately d=6.2 kpc, based on the morphological association with a molecular cloud. This is slightly farther than the previous distance, estimated to be 5 kpc (Lu et al. 2002). Here, we adopt the 6.2 kpc distance, which implies that $1'=1.8$ pc.

However, unlike the Crab, the diffuse X-ray emission in G54.1+0.3 extends well beyond the central X-ray torus/jet structures. This extensive, low surface brightness X-ray component corresponds well to the radio emission associated with this object. Reich et al. (1985) first identified G54.1+0.3 as a small-diameter ($1.5'$) radio source and suggested its nonthermal nature at 4.8 GHz. Velusamy & Becker (1988) present Very Large Array (VLA) of the National Radio Astronomy Observatory (NRAO)[1] observations of G54.1+0.3 at 4.8 and 1.4 GHz with resolutions of $5''$ and $14''$,

---

respectively. They confirm the nonthermal nature of the radio source, its center-filled morphology and linear polarization ($\sim$10%). The similarity of the extent of diffuse X-ray and radio emission also differs from that of the Crab, where the radio emission is much more extensive than the X-ray component. Similarities in the size of radio and X-ray PWNe have been observed in sources such as G292.0+1.8, the PWN powered by B1509-58, and 3C58 (Gaensler & Wallace 2003; Gaensler et al. 2002; Slane et al. 2004), and have interesting implications for the particle energetics and source structure.

Although detailed, multi-wavelength studies have been carried out for a growing number of PWNe (see recent review by Gaensler & Slane 2006), many issues relevant to Crab-like sources remain unresolved: (1) determining which acceleration mechanism can produce both the radio-emitting particles in addition the to the X-ray emitting particles is difficult (Atoyan 1999; Arons 2002; Bientenholz et al. 2004); (2) the absence of outer shells in many of these PWNe (e.g., 3C58 and the Crab). This question is related to the ages of the SNRs as well as the the properties of both the SN progenitors and the surrounding interstellar medium; and (3) the role and geometry of the magnetic field in the inner and outer regions of PWNe are not well-studied. Radio polarization studies have been carried out for a few PWNe (e.g., Crab, Vela, 3C58, G292.0+1.8, Boomerang) and show that the magnetic field structures in PWNe are highly-organized and often oriented radially toward the outer parts of the nebula. However, the transition from the predicted torodial magnetic field orientation at the very center of the PWN near the location of the pulsar (Bucciantini et al. 2005), to the outer, diffuse parts of the PWN has not been fully studied.

Because of its similarities (and important differences) to the Crab nebula, a multi-wavelength study of G54.1+0.3 can therefore provide insight as to many of the above unresolved issues. Understanding the nature of the diffuse X-ray emission and its relationship to the diffuse radio emission in G54.1+0.3 is crucial for understanding the energetic history of the PWN and its expansion into the surrounding interstellar medium. Archival VLA radio observations of G54.1+0.3 (Velusamy & Becker 1988) have relatively short integration times ($\sim$45 minutes at each frequency in the C array configuration) and low resolution (5-14$''$). Therefore, we present new multi-frequency, multi-configuration VLA observations of G54.1+0.3. These observations, which have resolutions of $\sim$3-5$''$, allow us to (1) characterize the radio emission on scales more comparable to the *Chandra* X-ray observations, (2) search for large-scale diffuse emission surrounding the central radio source, (3) study the radio spectral index variations across G54.1+0.3, (4) investigate the distribution and strength of polarized emission in G54.1+0.3, and (5) determine the Faraday rotation toward G54.1+0.3 and, ultimately, the intrinsic magnetic field structure of the PWN. The observations and data reduction are presented in §2, the results in §3, and the discussion and interpretation of results follow in §4.

2.   Observations and Imaging

VLA multifrequency observations of G54.1+0.3 were made during 2002-2004 using the B, C, and D array configurations at 1.4, 4.7 and 8.5 GHz. Table 1 summarizes the observational details.

At all frequencies, J1331+305 and J1924+334 were used as flux and phase calibrators. Standard procedures for calibration, editing and imaging were carried out using the Astronomical Image Processing Software (AIPS) of the NRAO. Data from different arrays were combined to produce final images at each frequency. Table 2 summarizes the image parameters. In order to measure flux densities, the images were corrected for primary beam attenuation, but the images shown in the paper have not been corrected for this attenuation as the correction causes the rms noise level to increase near the edges of the image, particularly at 8.5 GHz.

Polarization calibration was done for all three frequencies using the frequent observations of the phase calibrator J1924+334 in the B and C array observations. In the D array observations, polarization calibration was carried out only at 4.7 and 8.2 GHz; the 1.4 GHz observations did not have enough parallactic angle coverage for adequate polarization calibration. Stokes' Q and U images were made at 4.7 and 8.2 GHz and images of the polarized intensity ($I_p = \sqrt{Q^2 + U^2}$) were created. In order to study the Faraday rotation toward G54.1+0.3, additional Stokes' Q and U images were made at 4.585, 4.885, 8.085, and 8.465 GHz. For each of these IFs, images of the polarization angle ($PA = \frac{1}{2} Arctan(\frac{U}{Q})$) and the error in polarization angle were created. Using the polarization angle and error images at the four observed frequencies, the rotation angle as a function of wavelength was fitted to a λ^2 law with the AIPS algorithm RM. This task produces images of the distribution of the rotation measure and also the distribution of the orientation of the magnetic field intrinsic to the source by correcting the observed position angles for Faraday rotation.

3. Results

3.1. Radio Continuum Morphology

3.1.1. Structure of G54.1+0.3

Figures 1 and 2 show the detailed structure of the G54.1+0.3 radio source at 4.7 and 8.2 GHz. The radio continuum morphology at all frequencies (including 1.4 GHz) is nearly identical. The figures show that the source extends for approximately 2.5′ ×2.0′ (4.5 × 3.6 pc at d=6.2 kpc), with diffuse radio emission elongated in the NE-SW direction. The brightest emission is concentrated in the central 1-1.5′ area (1.8 to 2.7 pc), with intensities in this area of ∼1.5 mJy beam^{-1} at 4.7 GHz. The radio emission gets considerably weaker (∼0.1 mJy beam^{-1} at 4.7 GHz) moving outwards from the center of the nebula. Velusamy & Becker (1988) also note these same central features of the brightness distribution in their lower resolution observations.

The high resolution (∼3″) observations presented here reveal several new features in the morphology of G54.1+0.3. The brightness peaks near the center of G54.1+0.3, in several very pronounced ridges which appear to be tracing a ring or torus of ∼ 20−30″ diameter. In addition, there is a central cavity in the distribution of radio emission near RA, DEC (J2000): 19 30 30, 18 52 15. Slices of intensity across of the source indicate that the intensity in the central cavity is just

a fraction of that contained in the surrounding ridges: 0.7 mJy/beam compared to 1.3 mJy/beam at 8.5 GHz, (this trend in brightness is also observed at 4.7 GHz and 1.4 GHz). Figure 3 shows a slice of intensity across the center of G54.1+0.3. Velusamy & Becker (1988) also report on this decrease of intensity at the very center of G54.1+0.3, but did not have the resolution or sensitivity to distinguish the ring.

Figure 1 also reveals a number of filamentary structures in the NE and S portions of the nebula (labeled in Figure 1). In the NE part of G54.1+0.3, several elongated radio structures have sizes of $\sim$30-45$''$ (0.7-1 pc) near RA, DEC (J2000): 19 30 32, 18 52 15. Two of these features are mainly aligned with the NE-SW orientation of the radio nebula and suggestive of a flow. The third feature is oriented perpendicular to the NE-SW axis. In the southern part of the nebula, a number of loop-like structures are detected, ranging in size from 15-30$''$ (0.45-0.9 pc). Such filamentary and loop-like features are observed in the diffuse emission of several other PWNe, including both the Crab and 3c58, with similar physical sizes in all cases of 0.6 to 1 pc (Reynolds & Aller 1988; Velusamy 1985). Finally, G54.1+0.3 shows several "bays" to the NE and SW sides of the central ring or torus of radio emission which are similar to the optical bays in the Crab and 3C58 and the radio structure of PWN G21.5-0.9 (Furst et al. 1988; Velusamy 1985). These are discussed further in §4.6.

3.1.2. Diffuse Emission Surrounding G54.1+0.3

Since G54.1+0.3 lies in the Galactic plane, it is surrounded by diffuse large-scale radio emission. These larger structures are apparent in single-dish radio surveys of the Galactic plane (Caswell et al. 1985; Velusamy et al. 1986) but with resolutions of 1-3$'$, such images can not distinguish compact and shell-like features as in interferometric studies. Similar to the Crab, no shell surrounding G54.1+0.3 has ever been detected. Figure 4 shows the region surrounding G54.1+0.3 at 1.4 GHz; several shell-like radio sources and other large filamentary features are apparent in addition to the PWN which lies at the center of the image. In particular, a new radio shell-like structure has been detected (labeled in red in the figure) that appears to be centered around G54.1+0.3, with a diameter of $\sim$8$'$ (14.4 pc at 6.2 kpc). The radio shell is brightest on three sides of G54.1+0.3, with the faintest emission located in the SW portion of the shell. If the radio emission is nonthermal then this shell may be interpreted as the supernova remnant from the the G54.1+0.3 supernova explosion. However, determining the spectrum of the radio emission using the current interferometric data is difficult. At 4.7 GHz (image not shown; a larger field of view than Figures 1 and 2), extended emission is present to the NW and SE at approximately 8$'$ in radius from G54.1+0.3. At 1.4 GHz, there is considerably more diffuse emission in the field of view than at 4.7 GHz, presumably because of the better sensitivity to extended features. In fact, the largest angular size detectable with the VLA at 4.7 GHz is only 300$''$ (5$'$), so emission associated with this large ($\sim$8$'$) shell will not be observed with the VLA at this frequency. The brightest of the extended emission has an intensity of 100-200 μJy beam^{-1}, which corresponds to a signal-to-noise of $\sim$10 or less at best, and is not

well represented by the *(u,v)* coverage of the 4.7 GHz observation. Therefore we are unable to provide any reliable measure of the spectral index of the shell-like source surrounding G54.1+0.3. This shell is visible partly in the VLA Galactic Plane Survey image (D-array survey, $1'$ resolution) of Leahy et al. (2008), but it is on a much smaller scale than their large image (field of view ∼1 °). The nature of this shell is further discussed in §4.6.

3.2. Spectral Index of G54.1+0.3

Since we have detected G54.1+0.3 at three frequencies (8.2, 4.7 and 1.4 GHz), it is possible to derive the spectral index of the radio emission. The radio emission can be integrated over the entire source (a region of $\sim 2' \times 1.5'$). In all cases, the integrated flux density measurements have come from identical regions of G54.1+0.3. However, G54.1+0.3 lies in a crowded part of the Galactic plane (see above), many large scale extended features are present in 1.4 GHz image, which has a much larger field of view ($30'$) compared with the 4.7 or 8.2 GHz images (FOV $\sim$ 5-9$'$). The background flux levels in the 1.4 GHz image are much higher and variable over the image size than at other frequencies, and these variations contaminate the flux density measurements at 1.4 GHz. Therefore, we have corrected the 1.4 GHz measurement to yield $S_{1.4}$=433.0±30.0 mJy, $S_{4.7}$=327.0±25 mJy, and $S_{8.5}$=252.0 ±20.0 mJy. The average value of the integrated spectral index for G54.1+0.3 is α=−0.3±0.1. The spectral index between 1.4 GHz and 4.7 GHz has a value of α=−0.2±0.1 and between 4.7 and 8.5 GHz, α=−0.5±0.2. In addition, Figure 5 shows the spectrum of G54.1+0.3 based on the integrated flux density values and the best fit to this plot gives a spectral index value of α=−0.28.

In order to search for variations of the spectral index across the source, the spectral index can be calculated pixel by pixel across G54.1+0.3 using the AIPS task COMB (opcode=SPIX). Figure 6 shows the distribution of spectral index between 1.4 and 4.7 GHz in greyscale and overlaid by contours of 4.7 GHz continuum emission. This image was created by using data from matched arrays so that the spatial frequency sampling (i.e., *(u,v)* coverage) is consistent between both frequencies. In practice, this means that the 1.4 GHz image is constructed from B-array data only, the 4.7 GHz from C-array data only and the 8.2 GHz from D-array data only. Further, the spectral index images were obtained by convolving both images to the same resolution ($5''$) and determining the spectral index value at every pixel. The spectral index between 4.7 and 1.4 GHz in G54.1+0.3 does not show any variation across the nebula, with a fairly constant value of α=−0.2. The spectral index between 4.7 and 8.2 GHz also does not show any significant variation across G54.1+0.3, but has a slightly steeper average value, α=−0.3.

3.3. Polarization

There is strong linear polarization detected in G54.1+0.3 at both 4.7 and 8.5 GHz. The polarization at 1.4 GHz was significantly weaker ($\sim$10% fractional polarization) presumably because of bandwidth depolarization across the 50 MHz bandwidth at 1.4 GHz. Figure 7 shows polarized intensity at both 4.7 and 8.5 GHz. These figures illustrate that there is significant polarized intensity arising from G54.1+0.3 that closely follows the total intensity structure. The polarization is concentrated along the two central radio ridges, and the polarized intensity peak is offset by $\sim$10-15$''$ from the center of the PWN. Diffuse polarized intensity extends over much of the nebula. Figure 7 (top) shows that several of the radio loop-like features along the NW-SE extensions of the nebula are polarized. There are two striking linear features that extend for up to 30$''$ (0.9 pc) in extent; they are labeled in Figure 7 (top). The fractional polarization was sampled across the nebula and varies between $20-50\%$ at 8.2 and 4.7 GHz. Typical values of the fractional polarization are 27% at 8.2 GHz, 23% at 4.7 GHz. The highest values of fractional polarization are labeled in Figure 7 (bottom) and have values close to 40% at 8.5 GHz near RA, DEC (J2000): 19 30 30, 18 52 30.0 and 50% at 8.5 GHz near RA, DEC (J2000): 19 30 31, 18 52 50.0.

3.4. Rotation Measure and Intrinsic Magnetic Field Orientation

Figure 8 shows the distribution of rotation measure (RM) in rad m^{-2} toward G54.1+0.3, based on fitting the polarization angle as a function of wavelength squared (see §2) for interstellar Faraday rotation. Across much of the G54.1+0.3 nebula, the values for RM are in the range of 400-650 rad m^{-2}. In two regions (in the NE near RA, DEC (J2000): 19 30 33, 18 52 45, and in the SW near RA, DEC (J2000): 19 30 28, 18 52 15) the RM values appear to be lower by several hundred rad m^{-2}. Figure 9 shows a sample of the fits of polarization angle as a function of wavelength squared, where each panel represents the data averaged over a few pixels from two small regions of the source. The errors in the RM fits are on the order of 25-75 rad m^{-2}.

The vectors shown in Figure 10 represent the orientation of the magnetic field intrinsic to G54.1+0.3, obtained by correcting the observed polarization angles for the calculated RM. The magnetic field is very well ordered over the majority of the region which is polarized in G54.1+0.3 (see Figure 9, left). In particular, the magnetic field appears to follow closely the curvature of the central radio "ring" region. At the edges of the nebula, the magnetic field appears to be oriented along the linear extensions which are present in both total and polarized intensity and have a radial orientation. In the SE and SW portions of G54.1+0.3, the field becomes less-ordered as the polarized intensity fades.

4. Discussion

4.1. Comparison of Radio Emission and X-Ray Emission

Figure 11 shows a comparison of the 4.7 GHz radio emission in contours and the *Chandra* X-ray emission in colorscale (from Lu et al. 2002). The left panel has a colorscale stretch to emphasize the extended X-ray emission, and the right panel is set to emphasize the concentrated central X-ray emission. This figure, especially the left panel, illustrates that the distribution of large-scale and diffuse X-ray emission in G54.1+0.3 is strikingly similar to the extent of the radio emission. Figure 12 shows radial profiles of brightness taken along the NE (left) and SW (right) portions of G54.1+0.3. The dotted line illustrates the "edge" of the PWN in radio emission, corresponding approximately to the lowest radio contour level in Figure 11 (right panel). Although the X-ray emission drops more significantly than the radio emission, there is still diffuse and low-level X-ray emission arising from the same volume as the radio emission out to the lowest radio contour level.

However, in the center of the PWN, the radio and X-ray emission are not as well-correlated. The X-ray emission peaks at RA, DEC (J2000)= 19 30 30.1, 18 52 14.10, whereas the maximum in radio emission occurs at RA, DEC (J2000)= 19 30 30.5, 18 52 11.7. These positions are $\sim 6''$ apart. Figure 11 (top) shows that the peak in X-ray emission lies in a slight depression of radio emission, but with ridges of radio emission on either side. In addition, the projected orientation of the extended radio emission differs from the orientation of jet-like X-ray features (e.g., Figure 4 from Lu et al. 2002). These compact X-ray features in the center of G54.1+0.3 are oriented at angles of $\sim 45°$ with respect to the extended radio nebula (which runs along a NE to SW line). Apparently, the X-ray and radio emissions trace two rather distinct components of relativistic particles in the inner region of the PWN. While both emissions are apparently due to synchrotron radiation, their corresponding particle energies are very different (~ 100 TeV vs. ~ 1 GeV) and clearly represent different forms of pulsar injections and/or accelerations in the region.

Several PWN have been studied recently at high-resolution in the X-ray and radio: G0.9+0.1 (Dubner et al. 2008), 3C58 (Slane et al. 2004), G292.0+1.8 (Gaensler & Wallace 2003), and G21.5-0.9 (Furst et al. 1988; Bietenholz & Bartel 2008). G54.1+0.3 bears resemblance to several of these PWN, but is most similar to 3C58 in the following ways: (1) the substructure in G54.1+0.3 is filamentary and magnetized and (2) the extents of the diffuse radio and X-ray emission are comparable. Both 3C58 and G54.1+0.3 show evidence for filamentary and loop-like structures in X-ray and radio emission on size scales of 0.7-1 pc (e.g., in 3C 58 these structures are on size scales of 10-15$''$ for a distance of ~ 3 kpc and those scale directly to loop-like features of size 20-30$''$ in G54.1+0.3 at a distance of ~ 6 kpc). Slane et al. (2004) propose that the filamentary loops in 3C58 are magnetic loops torn from the toroidal field (associated with the pulsar) by kink instabilities. Figures 7 and 10 show that in G54.1+0.3 these filamentary loops are strongly polarized and have magnetic field orientations that align along their lengths. In fact, the curvature of magnetic structures that extend for as much as $15-30''$ are one of the more remarkable features of G54.1+0.3.

The overall diffuse structure of the radio and X-ray emission (that extends along the NE to SW line) in G54.1+0.3 closely resembles that of 3C58, in which the X-ray and radio emission fill essentially the same volume. Slane et al. (2004) report that the orientation of the elongation could be related to the toroidal magnetic field of the pulsar and that the elongation should line up with the orientation of the projected pulsar spin axis, as is roughly the case in 3C58. However, as described earlier there is a discontinuity between the orientation of the X-ray jet outflows and the extended radio emission in G54.1+0.3. Assuming that the pulsar spin axis is aligned with the X-ray jet-like feature, Ng and Romani (2004) estimate that the pulsar spin axis to be $\sim 90°$ with respect to N, or $\sim 45°$ with respect to the diffuse radio emission.

4.2. Source Energetics and Nebular Magnetic Field Strength

Figure 13 shows the spectrum of G54.1+0.3 over the range of $\sim 10^8$ to $\sim 10^{18}$ Hz. The flux in the diffuse X-ray emission is 5.2×10^{12} ergs cm^{-2} s^{-1}, which corresponds to 1.73 μJy. The radio spectrum (as discussed in §3.2 and shown in Figure 5) is relatively flat, with $\alpha_R = -0.28$, corresponding to a photon index (Γ)$=-1.28$. The diffuse X-ray nebula (not including the pulsar emission) has $\Gamma = -1.96 \pm 0.08$, or $\alpha_X \sim -0.96$. A spectrum was made and fit for this emission, defined by the "outer nebula" region from Lu et al. (2002). There is a trend in the diffuse X-ray emission, though, to soften outwards in the nebula: the inner X-ray ring has $\Gamma = -1.6$, and the photon index gradually decreases outwards in the nebula to nearly -2. This indicates that there is cooling in the X-ray particles as they extend to fill a similar volume as the radio particles. However, the X-ray index of uncooled particles, $\Gamma = -1.6$, is significantly steeper than the radio index. This shows that the responsible particles cannot be described by a single power law energy distribution.

According to Gaensler et al. (2002), the X-ray spectrum in PWNe are typically steeper than at radio wavelengths in part due to synchrotron losses which generate a break in the spectrum at the "break frequency". In this case, one can use Figure 13 to derive the break frequency. Figure 13 illustrates that the break frequency is the position where the two solid curves meet and occurs near $\nu_b = 50$ GHz for the X-ray spectrum of -0.96. However, the errors on the X-ray spectral fit give a large range of possible break frequencies, from $\nu_b = 3$ to 200 GHz. A variety of PWNe have been shown to have a steep spectral break at relatively low frequencies ($\nu_{break} < 100$ GHz; Woltjer et al. 1997); examples include 3C58 (Slane et al. 2004), G292.0+1.8 (Gaensler & Wallace 2003), and G21.5-0.9 (Bock et al. 2001) and G54.1+0.3 may be consistent with this class of PWNe. Here, we assume a break frequency from our radio and X-ray observations $\nu_b = 50$ GHz.

With a radio flux density of 327 mJy at 4.7 GHz, the $\alpha = -0.28$ spectral index and a distance of 6.2 kpc, the radio luminosity over the range of 10^7 Hz to 10^{11} Hz is 8.7×10^{32} erg s^{-1}. Over a similar range in frequency, the Crab has a radio luminosity of 1.8×10^{35} erg s^{-1}. The value for radio luminosity of G54.1+0.3 is several orders of magnitude below what has been found for many other PWNe, such as the Crab. What may be a more relevant quantity to compare is the ratio of radio luminosity to the spin-down power of the pulsar. For G54.1+0.3 this ratio ($L_R/\dot{E}$) is 8.7 x

$10^{32}/3.0 \times 10^{36} = 0.0003$. For the Crab, we calculcate almost exactly the same number: $L_R/\dot{E} = 1.8 \times 10^{35}/4.6 \times 10^{38} = 0.0004$.

The magnetic field strength in the PWN may play a role in regulating its expansion and in the energetics of the outflowing particles. If the break frequency is known or estimated, and the age of the PWN is known, then the nebular magnetic field can be calculated using the expression in Frail et al. (1996). The characteristic age $(P/2\dot{P})$ of the pulsar associated with G54.1+0.3 was determined to be 2900 years (Camilo et al. 2002). Using this age and the break frequency of 50 GHz, we estimate a magnetic field strength of $\sim$1250 μG. However, since the break frequency is not very well known, this estimate is more uncertain.

Alternatively, we can use the radio luminosity above and assume that there is equipartition between the particles and the magnetic field in the nebula. If we approximate the nebula as a sphere with diameter of 3.1 pc, then we derive an equipartition magnetic field strength of 38 μG. Another way to estimate the nebular magnetic field is by using the lifetime of the X-ray emitting particles. The particle flow velocity just down stream from the termination shock is derived by Lu et al. (2002) to be about v=0.4 c. Assuming a simple situation in which the flow is radial, we estimate a lifetime of 12.5 years (e.g., radius of PWN/the flow velocity). The lower limit on the mean flow velocity is unknown, but if we assume v=0.1 c, the lifetime of the particles will be 50 years. Then, assuming that the synchrotron lifetime at X-ray energies (i.e., $\sim$1.4 keV) depends on the magnetic field strength, we can derive a magnetic field in the nebula between 80-200 μG using the above velocities. Here, we understand that the magnetic field will be an upper limit as the particles may diffuse out to the edge of the nebula instead.

However, this magnetic field $-$ substantially higher than the equipartition magnetic field $-$ suggests that G54.1+0.3 is filled by a magnetically-dominated plasma, consistent with the presence of the polarization (and hence the magnetic field) organized on large scales of the nebula. Therefore, the magnetic field strength in G54.1+0.3 is probably stronger than the equipartition magnetic field, although the original wind from the pulsar is particle dominated (Lu et al. 2002). What might be the origin of this magnetic field? According to the convetional model for the Crab nebula (e.g., Kennel and Coroniti 1984), the pulsar wind is particle-dominated. But when it is terminated, the magnetic field is expected to be amplified in the down stream. The magnetic field can eventually become higher than the equipartition value. A detailed modeling, which accounts for the detailed magnetic field structure as reported here (see below), could potentially shed new light into the evolution and dynamics of the PWN.

4.3. Rotation Measure Distribution Toward G54.1+0.3

The fairly constant RM distribution across G54.1+0.3 indicates that we are detecting the Faraday rotation by the interstellar medium in the direction of G54.1+0.3 rather than an internal rotation process. There is a slight variation, however, of the RM, with larger values (near 500-600

rad m^{-2}) being concentrated toward the central $1'$ of the source and lower values (200-400 rad m^{-2}) concentrated outwards in the nebula. In particular, there are gradients in the RM in the NE and SW extents of the nebula where it is thought that the PWN may be interacting with a component of the interstellar medium (see below).

4.4.   Nature of the Magnetic Field Configuration in G54.1+0.3

Figure 7 shows that strong linear polarization is evident across much of G54.1+0.3 at both 8.5 and 4.7 GHz and that little change in polarized intensity morpholoy or fractional polarization occurs between frequencies. Because the polarization extends over much of the PWN, it is possible to determine the intrinsic magnetic field structure over this region. Studies that map out the intrinsic magnetic field have only been carried out for a handful of PWN sources (e.g., G106.6+2.9 (Kothes et al. 2006); Vela (Dotson et al. 2003); G21.5-0.9 (Furst et al. 1988), and G292.0+1.8 (Gaensler & Wallace 2003)). A large sample is needed to fully understand the magnetic field structure in these objects.

Kothes et al. (2006) present an interpretation of radio polarization measurements for G106.6+2.9, but generalized for many PWNe. They suggest that a toroidal field will appear to be tangential to the spin axis of the pulsar, whereas the radial field will appear along the elongation axis of the PWN. In many cases, the geometry will not be straightforward because of projection effects and the orientation of the observer. However, if the spin axis of the pulsar is known, then it is possible to imagine how the transition between the magnetic field in the inner region of the pulsar may be projected into something observable in the outer parts of the PWN.

In G54.1+0.3, the spin axis of the pulsar is assumed to be aligned roughly with the X-ray jets (i.e., Ng & Romani 2004), as in the Crab nebula and 3C58. Therefore, a toroidal field component would appear to be oriented perpendicular to this direction, and a radial magnetic field would align along this axis. Figure 14 shows the orientation of the intrinsic magnetic field vectors (in the plane of the sky) overlaid on greyscale representing the X-ray emission in G54.1+0.3. It is apparent that the majority of the magnetic field vectors are aligned in the central part of the nebula (where the X-ray emission is strongest) essentially tangential to the spin axis, but in the outer parts of the nebula, the field is radial and extends for the most part along the elongation. The exception is in the linear part of the loop-like feature in the NE part of the PWN. There appears to be a large magnetized loop emerging from this part of the PWN, perhaps an expanding part of the inner field structure. The difficulty with this is that the elongation of the diffuse nebula and the spin-axis from the X-ray are tilted with respect to each other, so this distribution of magnetic structure is complex. G54.1+0.3 appears to exhibit a complex radial magnetic field pattern, according to the classification of Kothes et al. (2006) by showing both radial and toroidal field components.

Finally, the role of the magnetic field in G54.1+0.3 may be similar to that in 3C 58. As described in the previous section, Slane et al. (2004) conclude that in 3C 58 the possible disruption

of a toroidal magnetic field configuration as the pulsar wind expands is responsible for producing the radio and X-ray "loops" and filamentary radio polarization structures. This may be the same mechanism at work in G54.1+0.3 where a toroidal magnetic field is present and may be disrupted in the outer parts of the nebula.

4.5.   New Radio Shell: Large-scale Emission Around G54.1+0.3

A clue to the nature of the new radio shell surrounding G54.1+0.3 can be gained by comparing the radio emission to the *Spitzer Space Telescope* 24 μm image made as part of the MIPS Legacy Project (MIPSGAL; Carey et al. 2009). The 24 μm emission traces stocastically-heated, small dust grains which trace massive stellar activity in the Galaxy. The radio continuum and 24 μm emission turns out to align very closely as evidenced in Figure 15. In addition to the large radio shell, Figure 15 also illustrates that there is a significant source of 24 μm emission associated with G54.1+0.3 itself that has a smaller, "loop-like" geometry ($80''$ or 2.4 pc across). This correspondance has been noted before by Koo et al. (2008) and Slane et al. (2008). Figure 16 shows archival *Spitzer* data (ID:3647) taken at 24μm pointed at G54.1+0.3 with radio continuum contours at 4.7 GHz overlaid. However, as pointed out in §3.1.2, the nature of the radio continuum emission is unclear and could be either free-free brehmstralung from ionized gas or nonthermal synchrotron emission.

Koo et al. (2008) indicate there may be some young stellar object (YSOs) sources and early B-stars embedded in the bright mid-infrared (mid-IR) loop that could be responsible for heating this large-scale radio shell (i.e., ionized gas). However, these ionizing sources may not be strong enough to account for the extensive radio emission in the radio shell if the total content of YSOs is on the order of $100M_\odot$ as suggested by Koo et al. (2008). In this case, the correspondance might represent the coincidence of a mid-IR shell with nonthermal radio emission. More sensitive multi-frequency radio observations which include the single dish flux are necessary to measure the spectral index accurately.

4.6.   Interplay of G54.1+0.3 with a Mid-infrared Cloud

As mentioned above, a more detailed view of the correlation between G54.1+0.3 and the mid-IR loop is shown in Figure 16 and reveals several morphological details: the bright radio ridges in the center of the PWN exactly fill a depression in the mid-IR loop, and the contours of radio emission, especially at the SW edge of the PWN very closely track the morphology of the mid-IR emission. In addition, an overlay between the X-ray emission in G54.1+0.3 and the 24 μm emission made by Slane et al. (2008) also reveals that the brightest X-ray emission concentrated in the central region of G54.1+0.3 is closely correlated with the edge of the mid-IR loop, indicating they may be interacting (see their Figure 3). Koo et al. (2008) have suggested that a burst of star-formation

evidenced by the presence of various near-to mid-IR sources (proposed to be massive YSOs), the formation of which may be triggered by the interplay of the stellar wind from the progenitor star of PWN G54.1+0.3. The large 24 μm luminosity and the presence of massive young stellar objects (Koo et al. 2008) indicate that the cloud is a pre-existing interstellar cloud, instead of part of the SN ejecta. It would also be difficult to imagine how the ejecta could remain so dense and cool in such a young SNR.

Several other features observed in G54.1+0.3 can be naturally explained with an interaction scenario: (1) the anti-correlation between peaks of the mid-IR emission and the distribution of RM (or similarly, polarized emission) shown in Figure 18. The polarization disappears abruptly at the edges of G54.1+0.3, before the radio continuum edge of the PWN, right at the positions where the thermal IR emission from the cloud appears to peak. In fact, closer inspection shows this change quite clearly: Figure 17 presents slices in fractional polarization at 4.7 GHz in (left) the SE part of G54.1+0.3, and (right) the SW part of G54.1+0.3 (see caption for exact locations of slices). In both cases, abrupt decreases in fractional polarization are detected before the edge of the radio continuum emission has been reached and coinciding with the peak of the mid-IR emission. In the case of the slice along the W side of G54.1+0.3, the fractional polarization falls off and then increases briefly again near the peak of the mid-IR emission. The sudden decreases in polarization can naturally be explained if the pulsar wind flow (hence, the magnetic field) changes direction because of the confinement of the mid-IR shell. (2) The change in direction of the pulsar wind flow will also have the effect of changing the orientation of the intrinsic magnetic field. Figures 10 and 14 show that the magnetic field becomes much less regular in the SW part of the PWN compared to the well-ordered and primarily radially-oriented fields in the N of the PWN. (3) Overall, the expansion of the PWN may be confined by the cloud which can explain the differences in the radio and X-ray emission. The brightest X-ray features are concentrated in the center of the PWN (see Figure 11 (top panel) and are dominated by the jets and central X-ray torus (e.g., Lu et al. 2002)). However, the diffuse X-ray emission and radio emission are well-aligned and their morphology is likely to be shaped by the ram-pressure confinement of thermalized particles. (3) The radio intensity contours (see Figure 16) appear to be compressed SW to the pulsar, relatively to the NE, which again can be a natural consequence of the ram-pressure confinement provided by the IR shell to the SW. There is no clear detection of the mid-IR cloud in existing ^{13}CO (1-0) data. One possibility is that the cloud could have been heated substantially and may be bright in higher order transitions. Sensitive observations of various molecular tracers are needed to further the study of the interplay between the G54.1+0.3 and the cloud.

The apparent confinement of G54.1+0.3 by the surrounding mid-IR cloud is somewhat similar to that of another PWN N157B in the Large Magellanic Cloud (Wang et al. 2001). In the case of PWN N157B, however, the confinement is probably due to the reflection of the supernova ejecta from a large-scale dense cloud, in contrast to the direct interaction of G54.1+0.3 with the mid-IR cloud. In both cases, the X-ray emission is largely extended, comparable to the radio emission in size, which is apparently caused by the bulk motion of pulsar wind materials due the direction

asymmetry in the ram-pressure confinement. The consideration of such bulk motion is important in understanding the evolution of the relativistic particles in the pulsar wind of G54.1+0.3 and the resultant X-ray and radio emission. Figure 19 shows a sketch of a possible interaction geometry between G54.1+0.3 and an interstellar cloud. The morphological "bays" mentioned earlier in the text and illustrated in Figure 1 are therefore likely to be more complicated that simple analogs to the bays in the Crab or in G21.5-0.9. The nature of the bays is far from clear and may be related to how the relativistic particles are injected from the pulsar and/or further accelerated in the nebula. The issue may also be complicated by the apparent confinement of the nebula by the mid-IR cloud.

In summary, this may be the first PWN where we are directly detecting its interplay with an interstellar cloud that has survived the impact of a supernova explosion. This interplay seems to give a natural explanation of the morphology and polarization change of the radio emission as well as its similarity and dissimilarity to the X-ray intensity distribution of the G54.1+0.3.

5. Conclusions

Here we summarize our radio observations of G54.1+0.3 and comparision with multi-wavelength observations of this source and draw the following conclusions:

(1) The higher resolution radio observations presented here reveal that G54.1+0.3 has a complex structure which closely resembles other PWNe (e.g., in particular, the Crab, 3C 58, and G.21.5-0.9). G54.1+0.3 shows wispy and filamentary radio structures in the outer parts of the nebula that are loop-like and are polarized. On large scales, the radio emission in G54.1+0.3 is extended along the NE−SW direction. The radio emission in the center of the nebula is concentrated into a ring or torus-like object with a larger radius that the X-ray torus.

(2) Comparisons between G54.1+0.3 in the radio and X-ray are striking as there is much similarity at these two different frqeuencies. Both the radio and X-ray emission have comparable diffuse extents with the presence of filamentary and loop-like structures as mentioned above. However, the inner part of G54.1+0.3 is dominated by bright X-ray emission associated with the jet-like features. These structures are offset from the central radio features, which peak further outwards in the nebula than the X-ray emission. The radio emission also tends to dominate the nebula on larger scales.

(3) No spectral index gradient is detected in the radio emission across the PWN, whereas the X-ray emission softens outward in the nebula, consistent with the synchrotron cooling of the X-ray-emitting particles in a magentic field of about 100 μG.

(4) The strong radio polarization present in G54.1+0.3 allows us to image in detail the intrinsic magnetic field across the PWN. Clear radial and toroidal components of the magnetic field are detected in G54.1+0.3, which is an intermediate morphology for the field, according to the classification scheme of Kothes et al. (2006).

(5) Strong mid-IR emission from a bright loop is closely correlated with the southern edge of G54.1+0.3. In particular, the distribution radio and X-ray emission compared with the mid-IR emission suggest that the PWN may be interacting with this interstellar cloud. Figure 19 shows a sketch of such a possible interaction.

(6) An interaction between the PWN G54.1+0.3 and the interstellar cloud (traced in mid-IR emission) may naturally explain the differences in the orientation of X-ray and radio emission in G54.1+0.3, the change of magnetic field orientation and the RM distribution and the apparent compression of the radio emission along the southern part of G54.1+0.3. This may be the first PWN where we are directly detecting its interplay with an interstellar cloud that has survived the impact of the supernova explosion associated with the pulsar's progenitor.

REFERENCES

Atoyan, A. M. 1999, A&A, 346, L49

Arons, J. 2002, in *Neutron Stars in Supernova Remnants*, ASP Conference Series, ed. P. Slane and B. Gaensler, 271, 71

Begelman, M. C. 1998, ApJ, 493, 291

Caswell, J. L. 1985, AJ, 90, 1224

Bucciantini, N., del Zanna, L., Amato, E., & Volpi, D. 2005, A&A, 443, 519

Camilo, F., Lorimer, D. R., Bhat, N. D. R., Gotthelf, E. V., Halpern, J. P., Wang, Q. D., Lu, F. J., & Mirabal, N. 2002, ApJ, 574, L71

Carey, S.J., et al. 2009, PASP, 121, 76

Chen, Y. et al., 2006, ApJ, 651, 237

Chevalier, R.A., 2002, in *Neutron Stars in Supernova Remnants*, ASP Conference Series, 271, 125

Frail, D. A., Giacani, E. B., Goss, W. M., & Dubner, G. 1996, ApJ, 464, L165

Furst, E., Handa, T., Morita, K., Reich, P., Reich, W., & Sofue, Y. 1988, PASJ, 40, 347

Gaensler, B. M., Arons, J., Kaspi, V. M., Pivovaroff, M. J., Kawai, N., & Tamura, K. 2002, ApJ, 569, 878

Gaensler, B. M., & Wallace, B. J. 2003, ApJ, 594, 326

Gaensler, B. M., & Slane, P. O. 2006, ARA&A, 44, 17

Kennel, C. F., & Coroniti, F. V. 1984, ApJ, 283, 694

Koo, B.-C., et al. 2008, ApJ, 673, L147

Kothes, R., Reich, W., & Uyaniker, B. 2006, ApJ, 638, 225

Leahy, D. A., Tian, W., & Wang, Q. D. 2008, AJ, 136, 1477

Lu, F. J., Wang, Q. D., Aschenbach, B., Durouchoux, P., & Song, L. M. 2002, ApJ, 568, L49

Ng, C.-Y. & Romani, R. 2004, ApJ, 601, 479

Rees, M. J., & Gunn, J. E. 1974, MNRAS, 167, 1

Reich, W., Fuerst, E., Altenhoff, W. J., Reich, P., & Junkes, N. 1985, A&A, 151, L10

Reynolds, S. P., & Aller, H. D. 1988, ApJ, 327, 845

Reynolds, S. P., & Chevalier, R. A. 1984, ApJ, 278, 630

Slane, P., Helfand, D., van der Swaluw & Murray, S. 2004, ApJ, 616, 403

Slane, P. 2008, Conf. proceedings for *Astrophysics of Compact Objects*, AIP Conf.Proc.968:143-150

Velusamy, T. 1985, MNRAS, 212, 359

Velusamy, T., Goss, W. M., & Arnal, E. M. 1986, Journal of Astrophysics and Astronomy, 7, 105

Velusamy, T., & Becker, R. H. 1988, AJ, 95, 1162

Wang, Q. D., Gotthelf, E. V., Chu, Y.-H., & Dickel, J. R. 2001, ApJ, 559, 275

Woltjer, L., Salvati, M., Pacini, F., & Bandiera, R. 1997, A&A, 325, 295
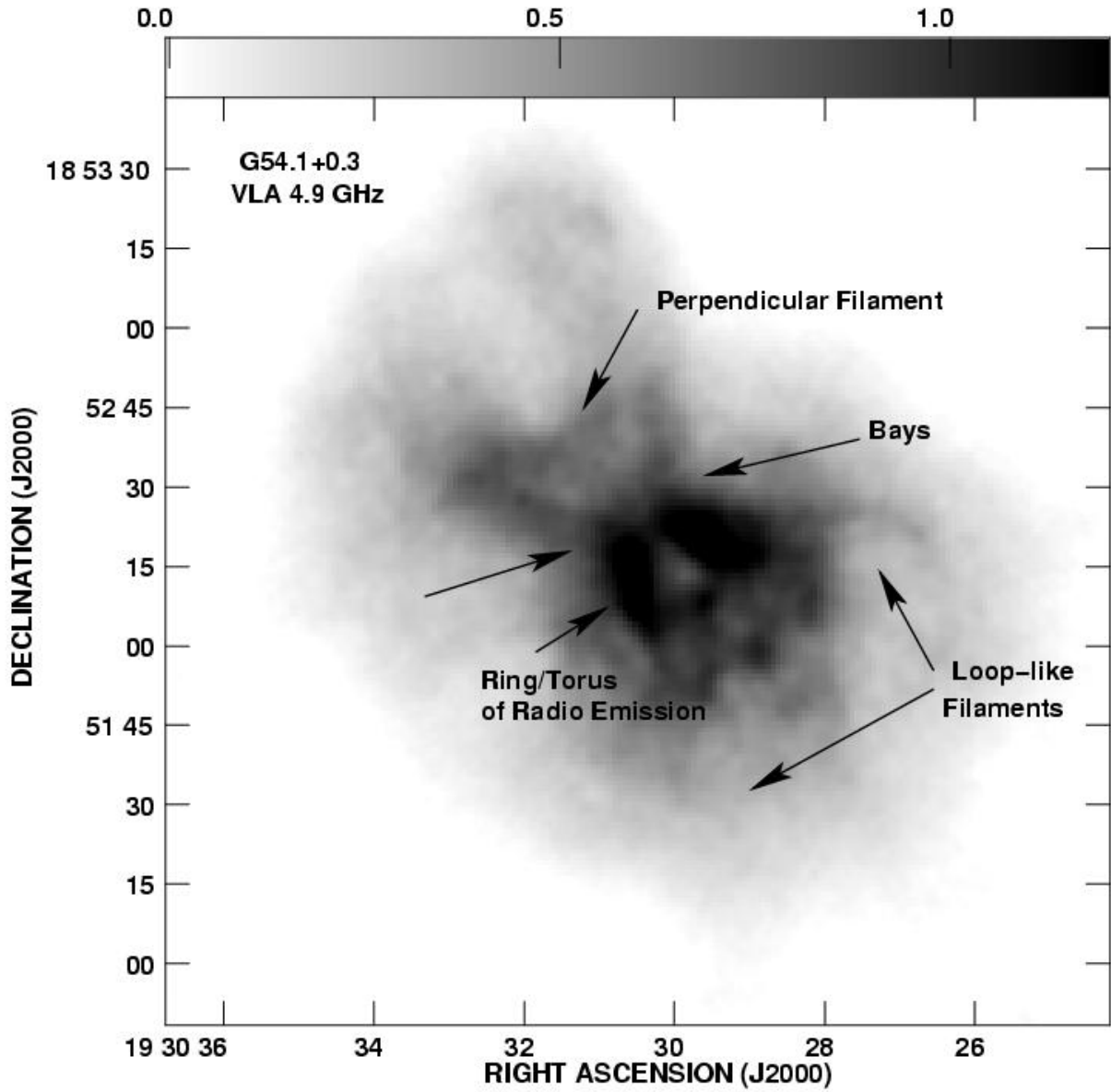
Fig. 1.— VLA 4.7 GHz continuum image of G54.1+0.3 shown in greyscale representing 0 to 1.25 mJy beam^{-1} (see axis on top of figure for greyscale range in mJy beam^{-1}). The resolution of this image is 3.28″ ×3.21″, PA=−41.6° and the rms noise is 15 μJy beam^{-1}.
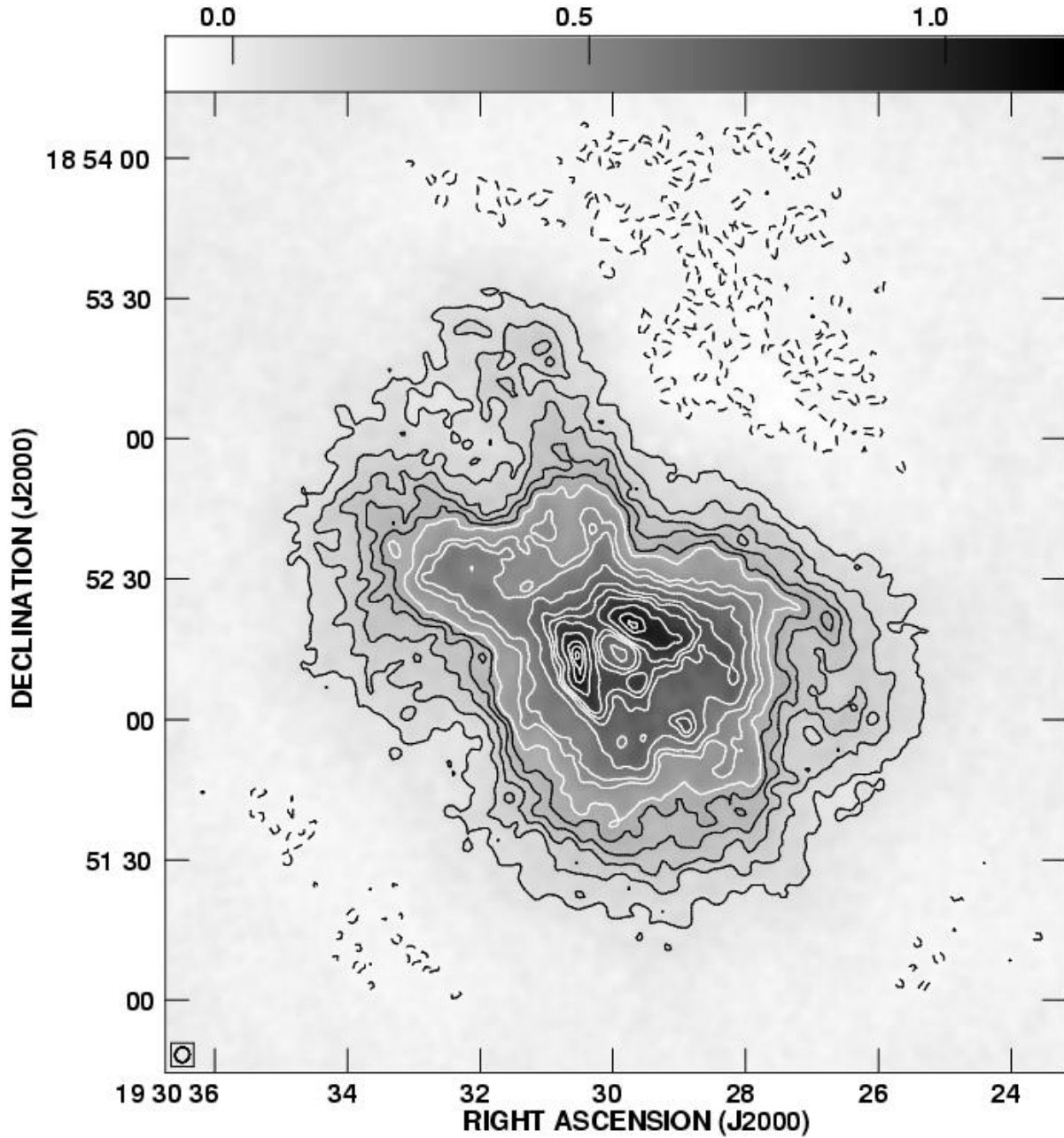
Fig. 2.— VLA 8.2 GHz continuum image of G54.1+0.3 shown in greyscale representing 0 to 1.25 mJy beam^{-1} (see axis on top of figure for greyscale range in mJy beam^{-1}) and contour levels representing -5, 5, 10, 15, 15, 20, 25, 30, 40, 45, 55, 65, 70, 75, 85, 95, 100 and 104 times the rms level of 10 μJy beam^{-1}. The resolution of this image is $3.22''\times3.01''$, PA$=-20.0°$.
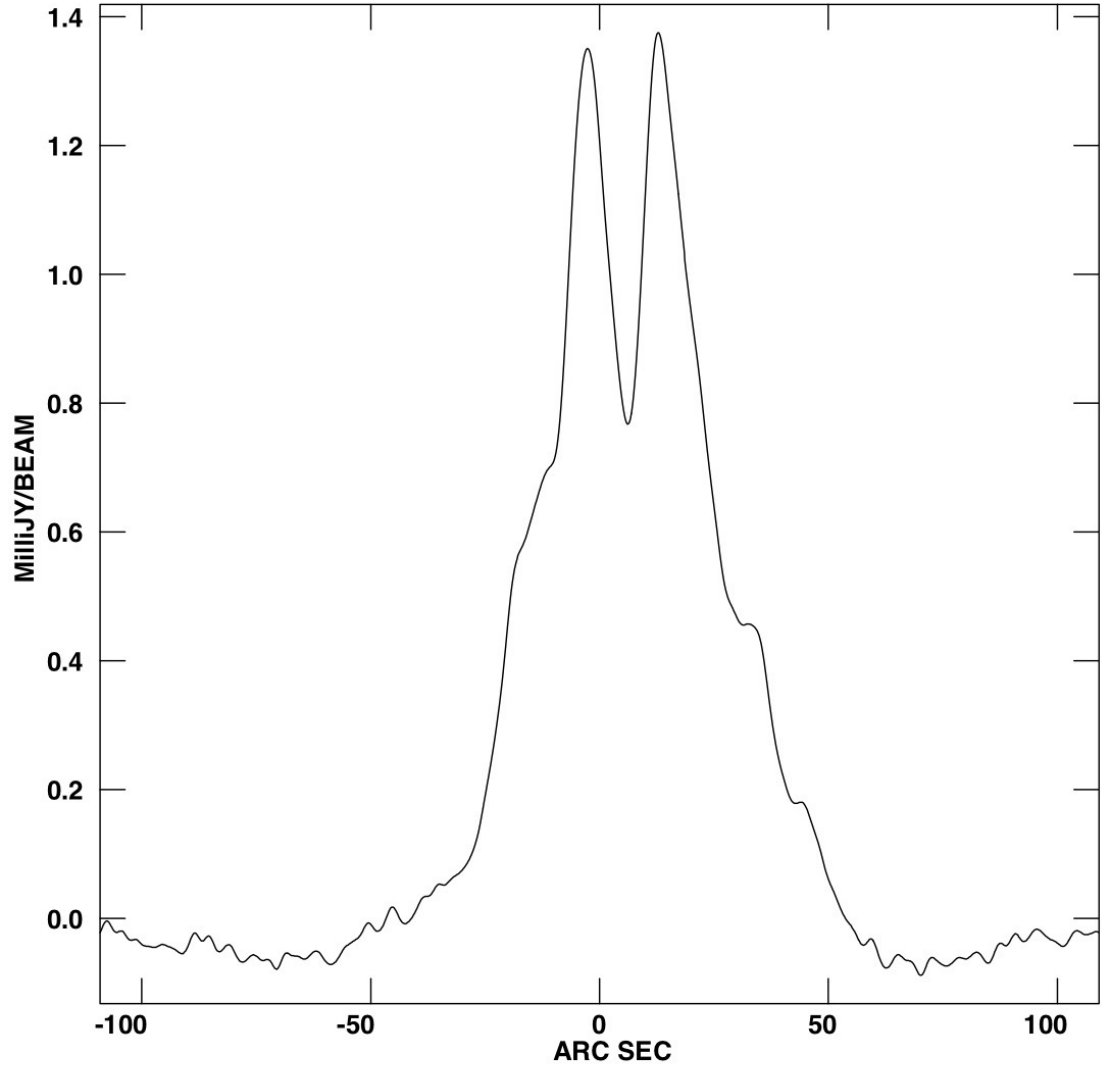
Fig. 3.— VLA 8.5 GHz radio continuum intensity as function of position (in arcseconds) across G54.1+0.3. This slice was taken through the broadest part of the radio "ring/torus" on a line that is at a 45° angle (E of N). The beginning point is RA, DEC (J2000): 19 30 34, 18 51 45, and the end point is RA, DEC (J2000): 19 30 26, 18 53 00. This figure illustrates that the central radio emission is concentrated in a ring-like distribution.
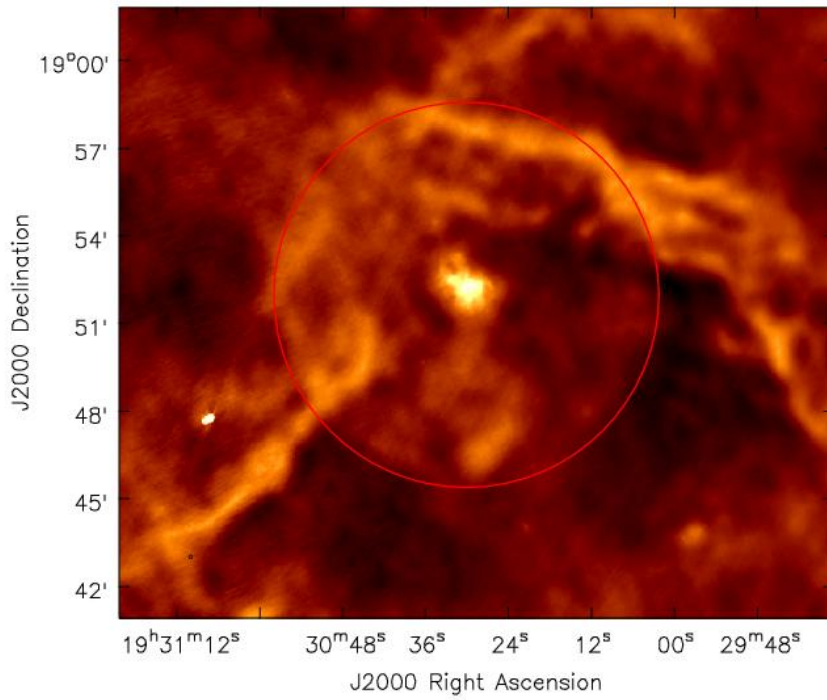
Fig. 4.— VLA 1.4 GHz continuum image of the region surrounding the compact source G54.1+0.3, with a resolution of $6.82'' \times 6.60''$, PA=5.5°. The new radio shell is marked in the figure.
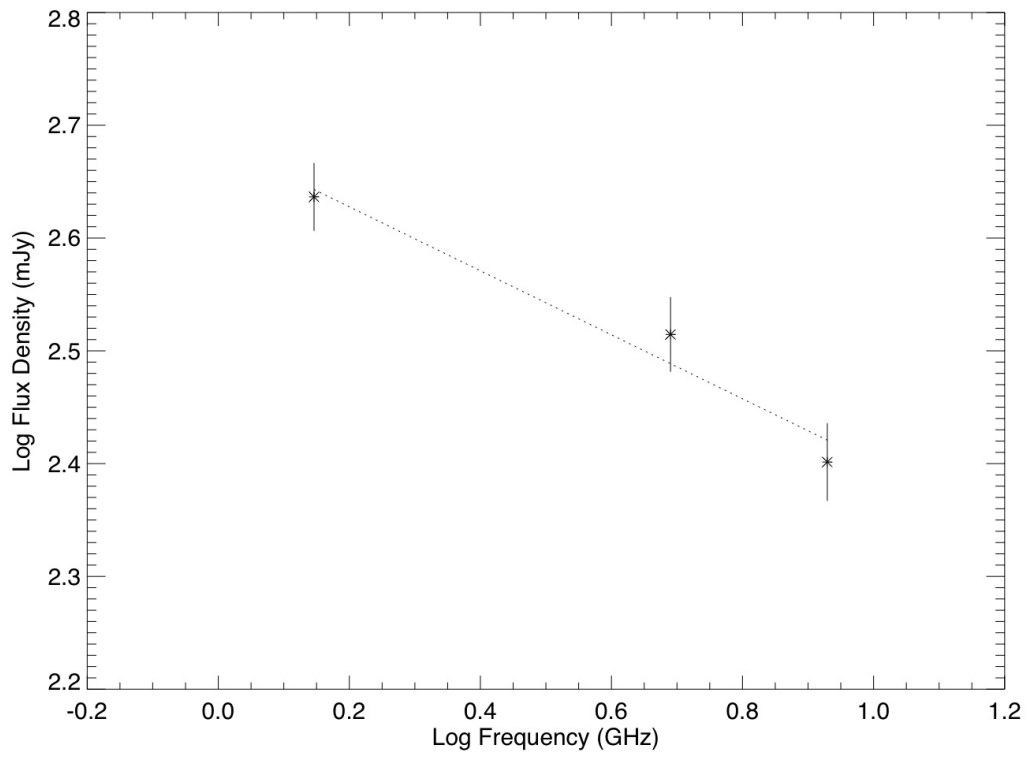
Fig. 5.— Radio spectrum of G54.1+0.3, based on flux densities measured at 1.4, 4.7 and 8.2 GHz and shown with errors. The dotted lines represent the best fit to the spectral index.
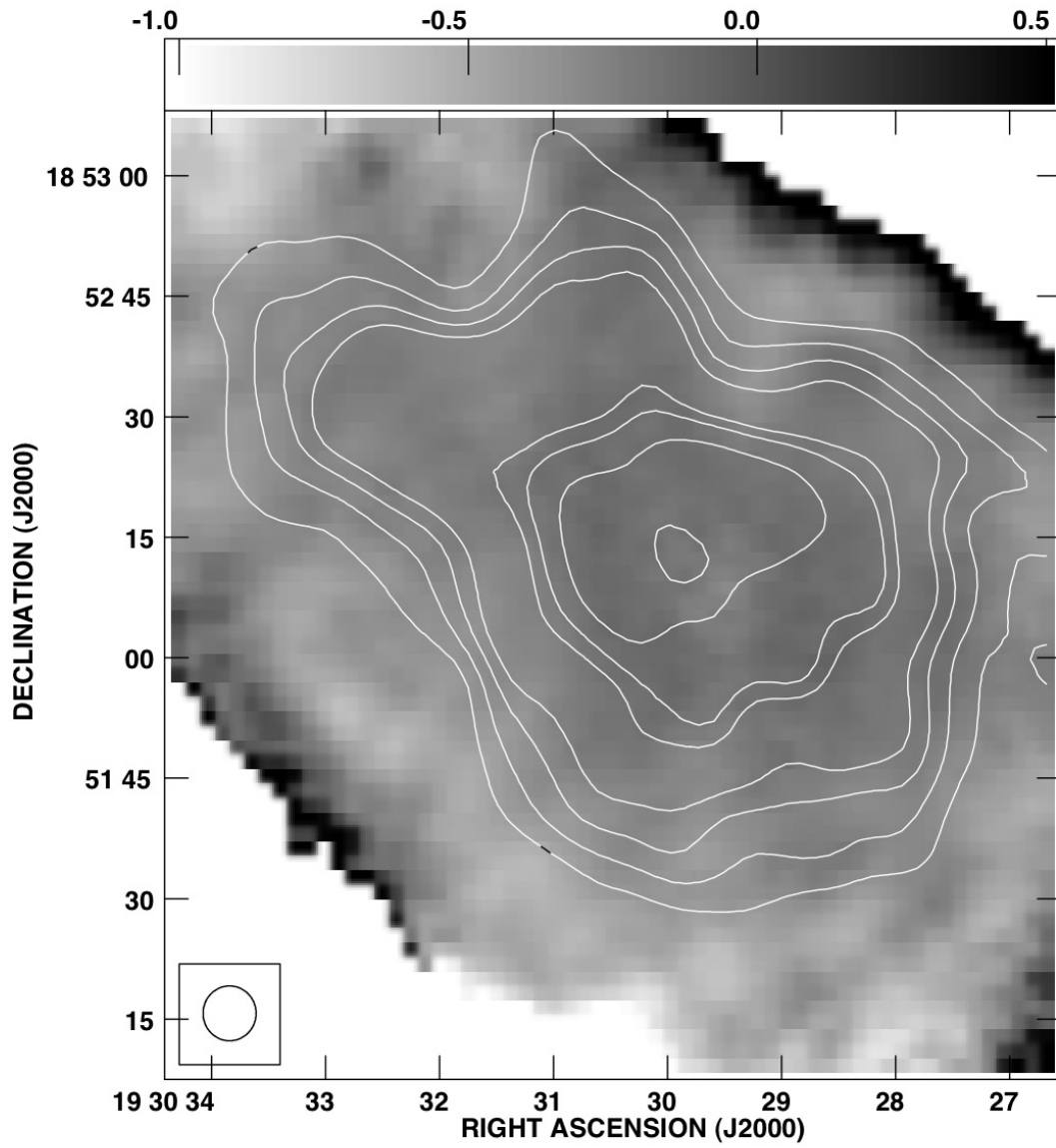
Fig. 6.— VLA 4.7 GHz continuum continuum contours of G54.1+0.3 shown overlaid on greyscale representing the 1.4 to 4.7 GHz spectral index, with greyscale that ranges from $\alpha=+0.5$ to -1.0.
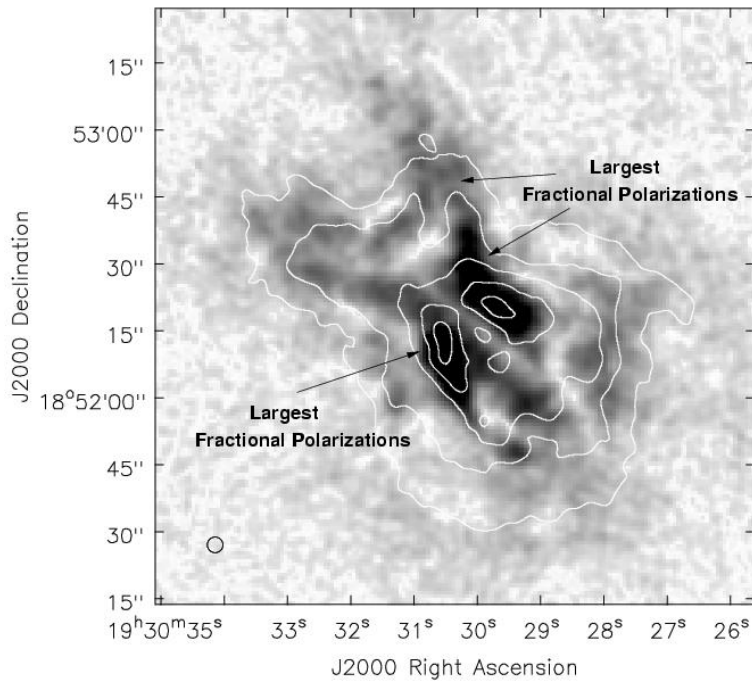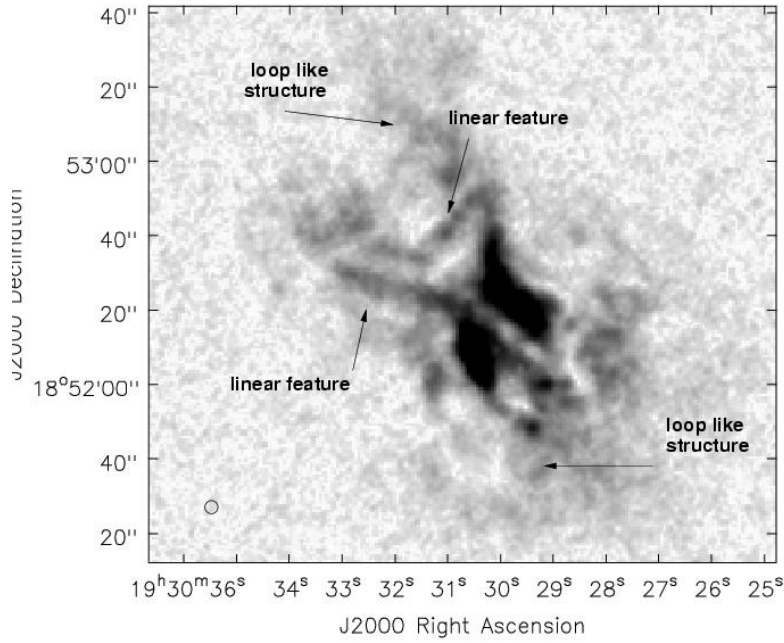
Fig. 7.— Polarized intensity images shown in greyscale, which ranges from 0 to 200 μJy beam^{-1}, and have resoltions of $3.5'' \times 3.5''$ at **(top)**: 4.9 GHz and **(bottom):** 8.2 GHz overlaid with contours of total intensity at levels of 0.25, 0.5, 0.75, 1.0, and 1.25 mJy beam^{-1}.
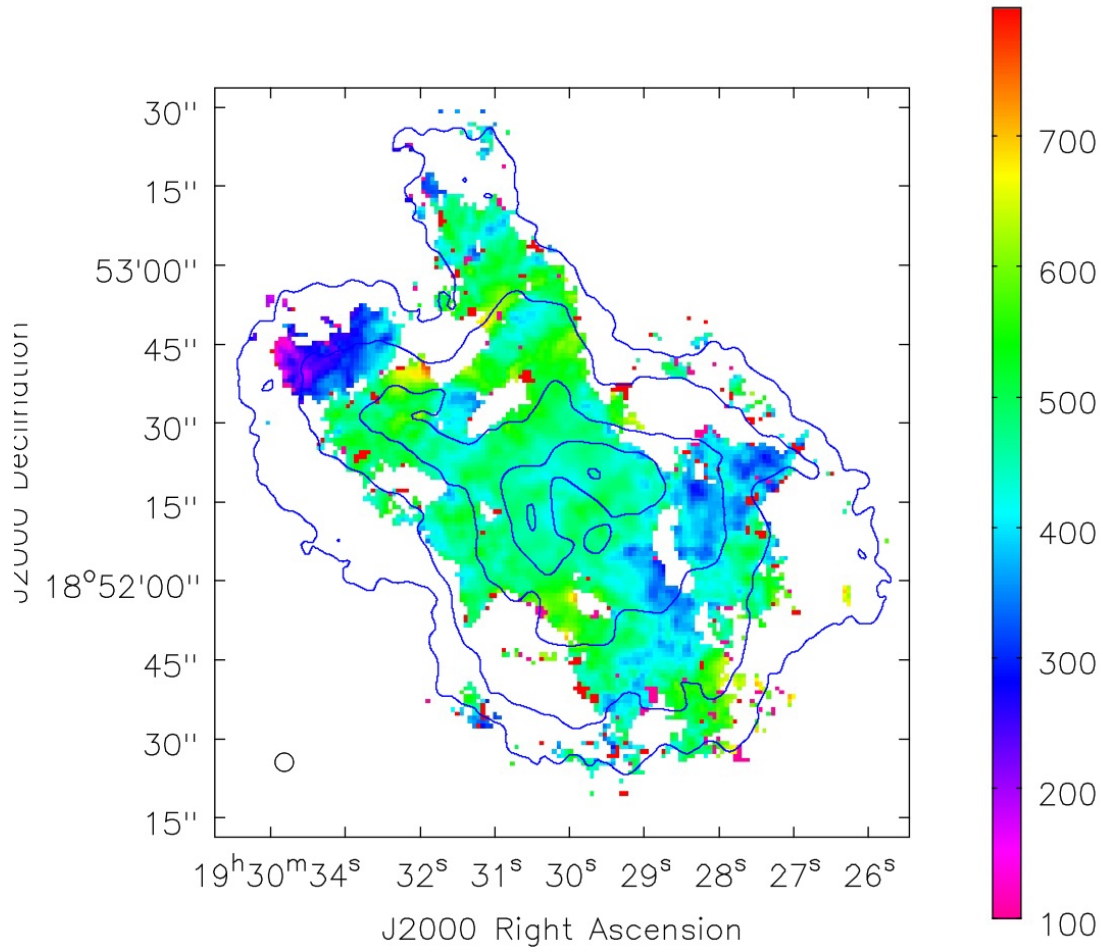
Fig. 8.— Colorscale representing the distribution of rotation measure (RM) toward G54.1+0.3 in units of 100-500 rad m^{-2}, with a spatial resolution of $3.5''\times3.5''$.
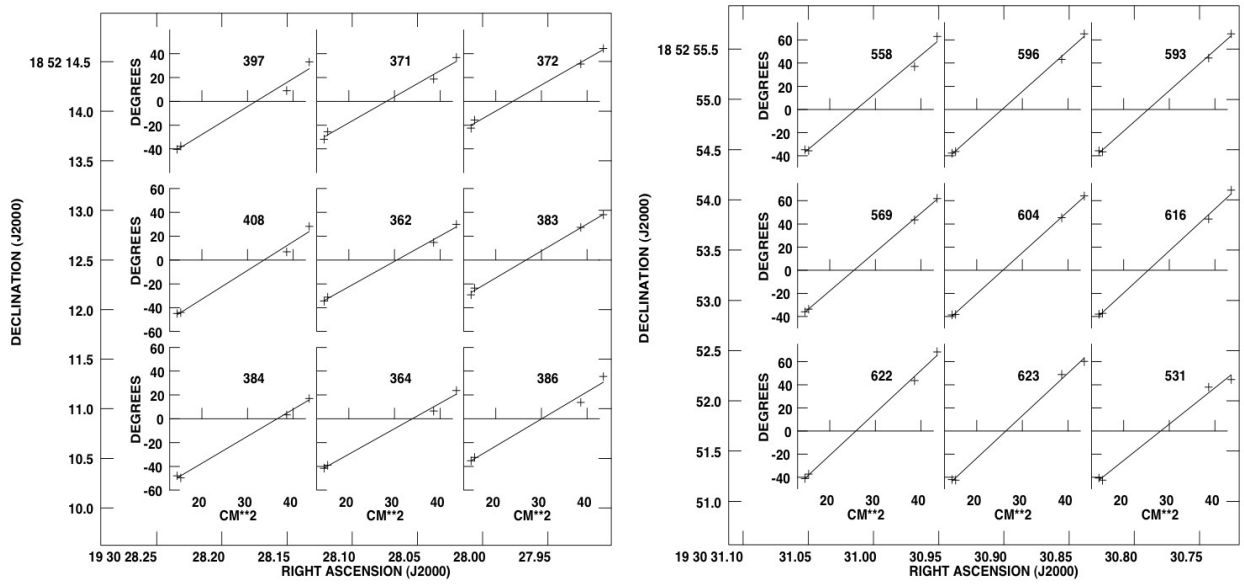
Fig. 9.— Polarization rotation angle versus wavelength squared for two regions in G54.1+0.3.
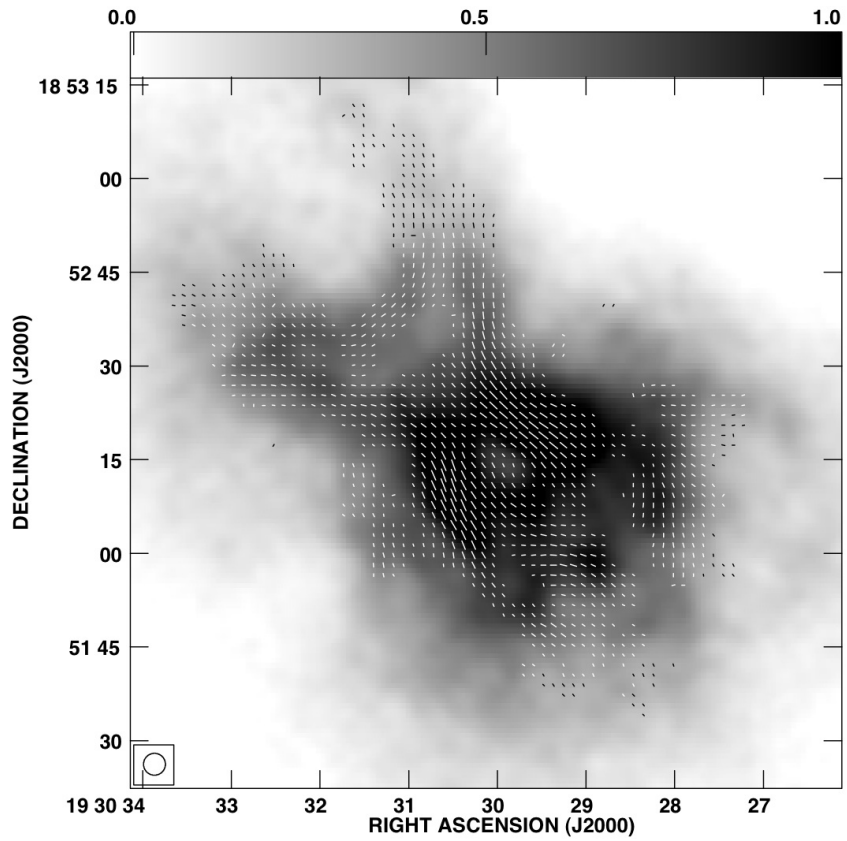
Fig. 10.— Vectors of the intrinsic magnetic field orientation in G54.1+0.3 overlaid on greyscale representing 8.5 GHz emission between 0 and 1.0 mJy beam^{-1} (see top axis).
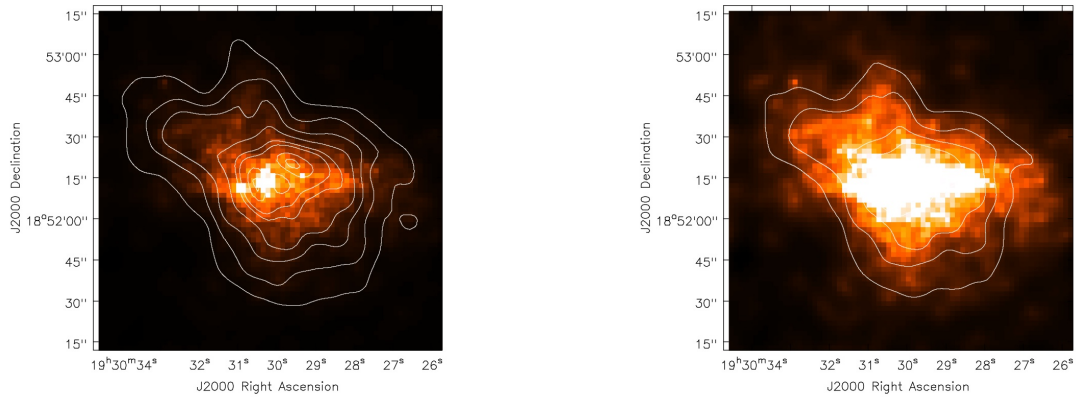
Fig. 11.— Comparison of radio emission (4.7 GHz data from this study; see Figure 1) and X-ray emission from the *Chandra* X-ray observatory (Lu et al. 2002). The top image has a color stretch selected to show the centrally-concentrated X-ray emission for comparison with the radio emission in the nebula, and the bottom image has a color stretch set to highlight the diffuse X-ray emission which fills the same volume as the radio nebula.
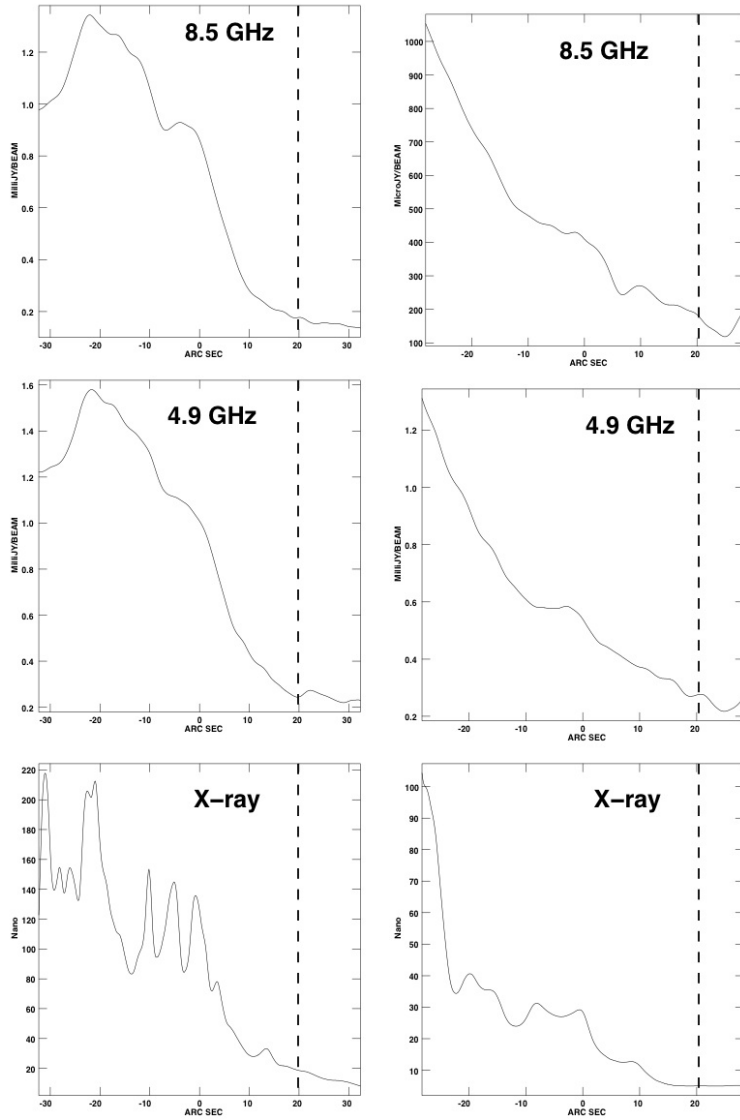
Fig. 12.— Comparison of the radio and X-ray extent of G54.1+0.3. The upper panels are radio frequencies (4.7 and 8.5 GHz) and the bottom panels are X-ray emission. The brightness profiles show a radial slice from the center of the nebula outwards at two different locations. The dashed line marks the edge of the radio nebula.
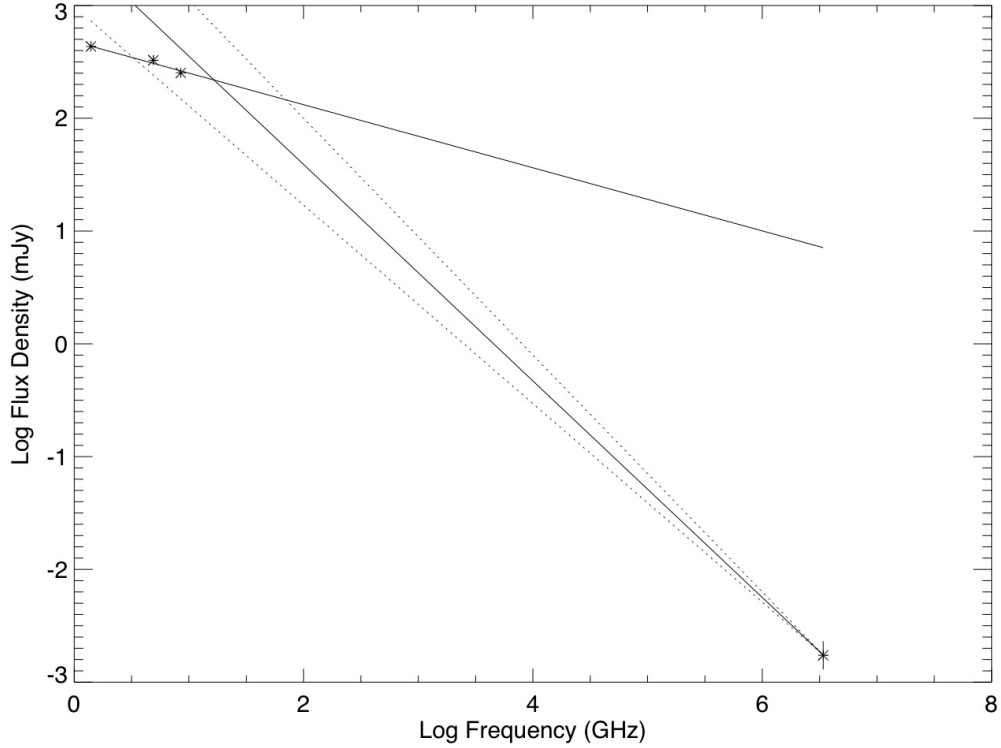
Fig. 13.— Spectrum of the G54.1+0.3 PWN over the radio to X-ray regime, with the radio spectrum ($\alpha_R = -0.28$) shown as a solid line, and the X-ray spectrum ($\alpha_X = -0.96$) shown with a solid line. The position where these two curves meet is known as the break frequency and occurs near $\nu_b = 50$ GHz. However, the errors on the X-ray spectral fit give a large range of possible break frequencies, from $\nu_b = 3$ to 200 GHz.
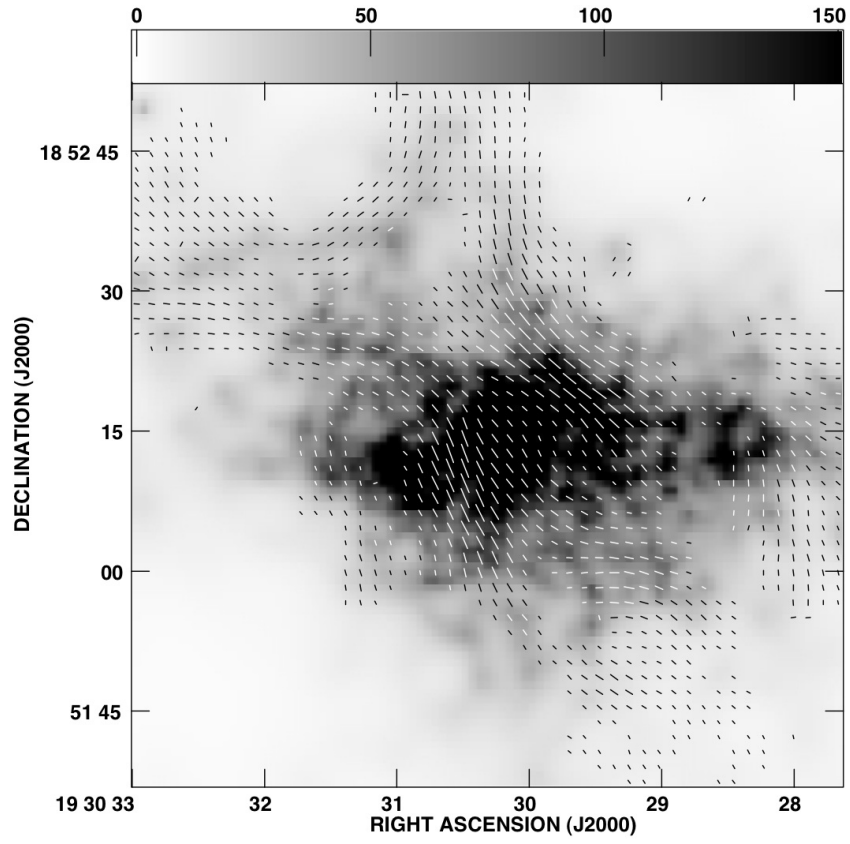
Fig. 14.— Vectors of the intrinsic magnetic field orientation in G54.1+0.3 from these data (presented in Figure 10) overlaid on greyscale showing the 0.2-10 keV X-ray emission from Lu et al. (2002).
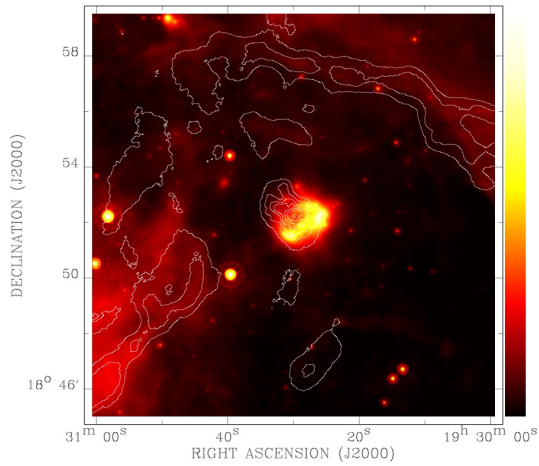
Fig. 15.— Comparison of the large-scale structure surrounding G54.1+0.3 showing 1.4 GHz radio emisson (white contours) and the *Spitzer* 24 μm data from the MIPSGAL survey (Carey et al. 2009). G54.1+0.3 is the compact object in the middle of the image in green contours and the colorscale shows the new shell of radio emission in addition to the local galactic background. This image is shown in Galactic coordinates.
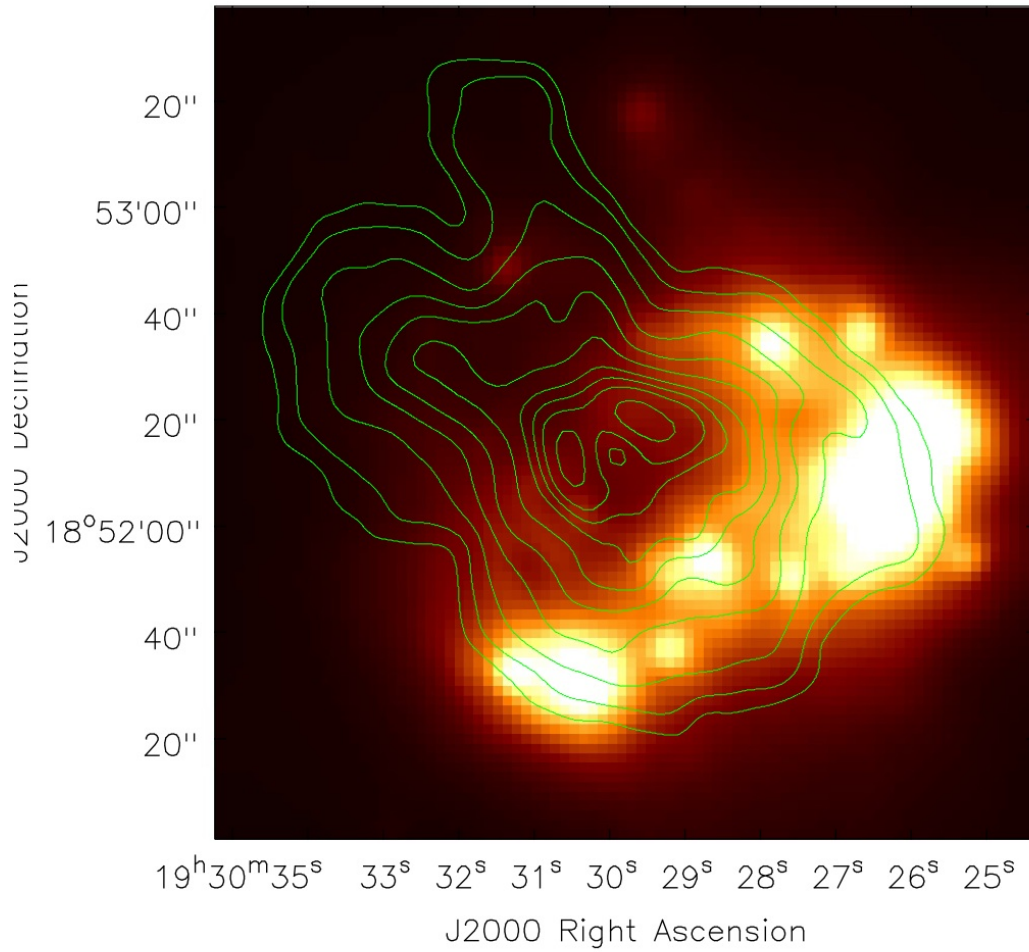
Fig. 16.— Zoomed-in view of the comparison of radio continuum emisson (contours of 4.7 GHz emission) and colorscale showing *Spitzer* 24 μm data from the archive (program=3647).
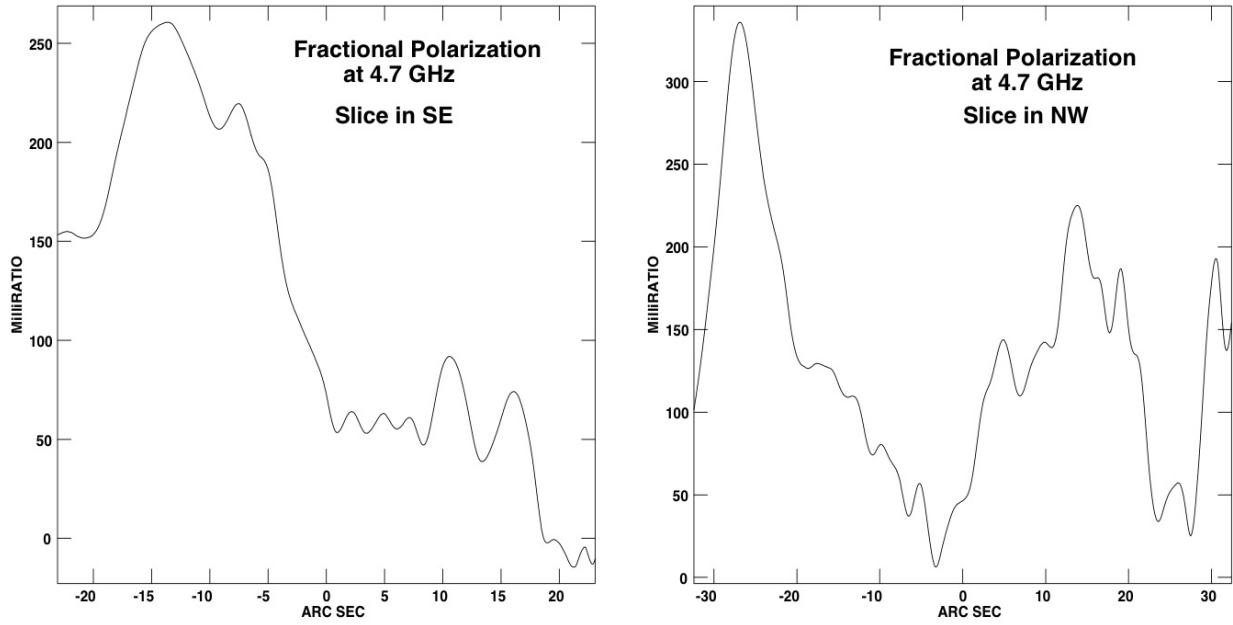
Fig. 17.— Slices in fractional polarization at 4.7 GHz (polarized intensity/total intensity) across G54.1+0.3. (left) Slice in the SE part of the PWN beginning near the center of the source near RA, DEC (J2000): 18 52 15, 19 30 31, and extending essentially south to RA, DEC (J2000): 18 52 45, 19 30 30. (right) Slice originating at the center of the PWN near RA, DEC (J2000): 18 52 30, 19 30 30 and extending essentially eastward to the edge of the nebula at RA, DEC (J2000): 18 52 15, 19 30 28. In this slice, it is clear that the polarization falls off, then increases again before the edge of the PWN.
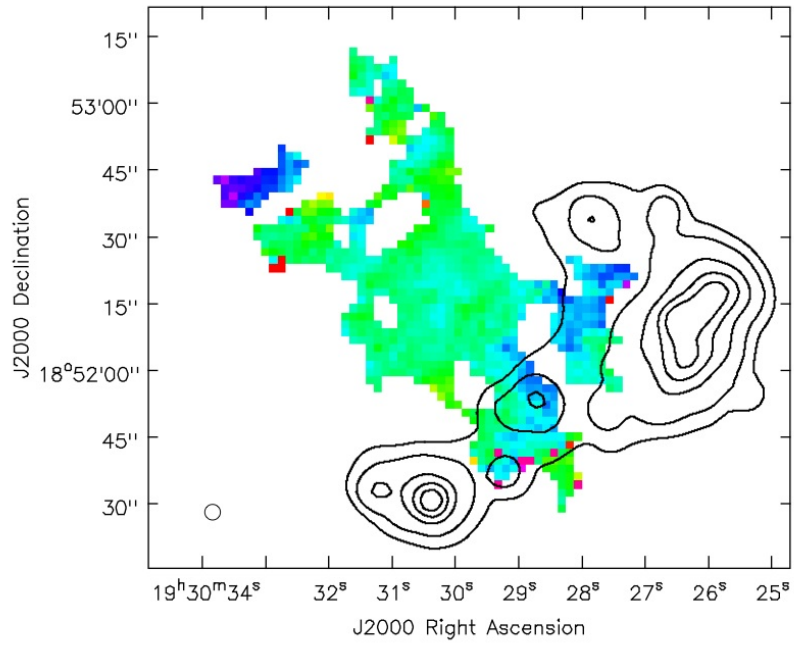
Fig. 18.— Distribution of rotation measure in rad m^{-2} (as shown in Figure 8) with contours of 24 μm emission from the *Spitzer* archive (program=3647) overlaid. What is notable here is the anti-correlation between the rotation measure and the intensity of 24 μm emission.
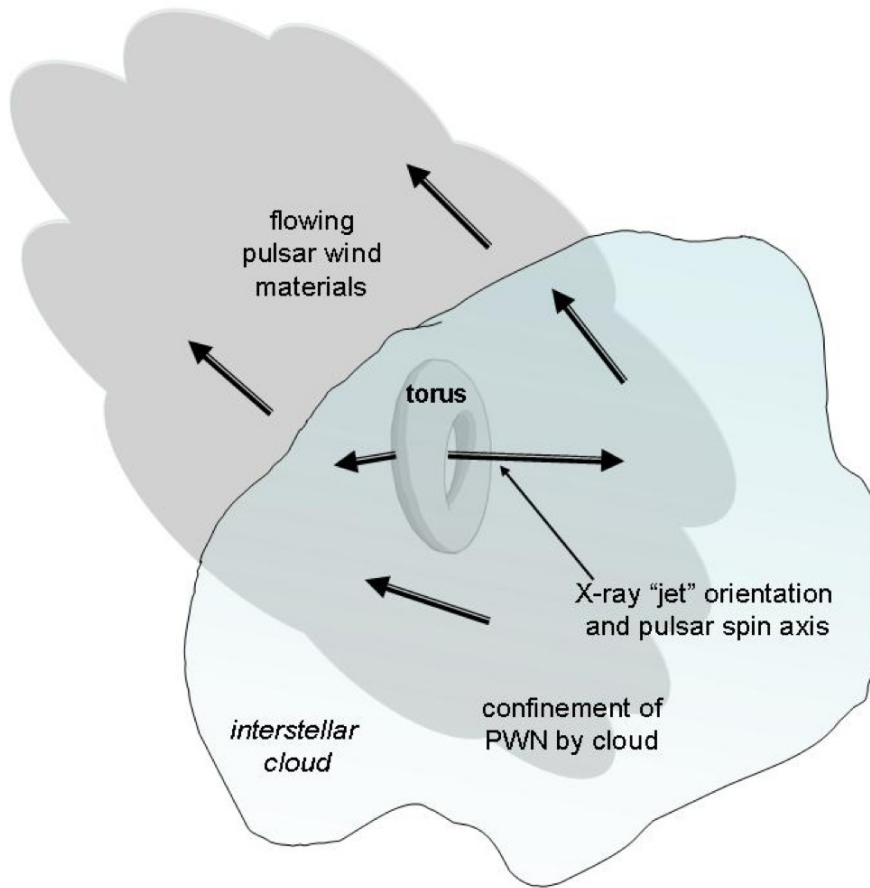
Fig. 19.— Sketch of a possible scenario for the interaction of G54.1+0.3 with an interstellar cloud.